Ultracompact H II regions with extended emission: the case of G43.89–0.78 and its molecular environment

Eduardo de la Fuente [ORCID],[1][*][†] Daniel Tafoya,[2] Miguel A. Trinidad,[3] Alicia Porras,[4] Alberto Nigoche-Netro,[5] Simon N. Kemp,[5] Stanley E. Kurtz,[6] José Franco[7] and Carlos A. Rodríguez-Rico[3]

[1]*Departamento de Física, CUCEI, Universidad de Guadalajara, Blvd. Gral. Marcelino García Barragán 1421, Olímpica, Guadalajara, Jalisco 44430, México*
[2]*Department of Space, Earth and Environment, Chalmers University of Technology, Onsala Space Observatory, Onsala 43992, Sweden*
[3]*Departamento de Astronomía, Universidad de Guanajuato, Apartado Postal 144, Guanajuato 36000, México*
[4]*Instituto Nacional de Astrofísica, Óptica y Electrónica, Luis E. Erro Número 1, Tonantzintla, San Andrés Cholula, Puebla 72840, México*
[5]*Instituto de Astronomía y Meteorología, CUCEI, Universidad de Guadalajara, Av. Vallarta 2602, Guadalajara, Jalisco 44130, México*
[6]*Instituto de Radioastronomía y Astrofísica, UNAM, Antigua Carretera a Pátzcuaro Numero 8701, Morelia, Michoacán 58089, México*
[7]*Instituto de Astronomía, UNAM, Apartado Postal 70-264, CDMX 04510, México*

ABSTRACT

The Karl Jansky Very Large Array (VLA), Owens Valley Radio Observatory (OVRO), Atacama Large Millimetric Array (ALMA), and the infrared *Spitzer* observatories are powerful facilities to study massive star formation regions and related objects such as ultra-compact (UC) H II regions, molecular clumps, and cores. We used these telescopes to study the UC H II region G43.89–0.78. The morphological study at arcminute scales using NVSS and *Spitzer* data shows that this region is similar to those observed in the *bubble-like* structures revealed by *Spitzer* observations. With this result, and including a physical characterization based on 3.6 cm data, we suggest G43.89–0.78 be classified as an UC H II region with Extended Emission because it meets the operational definition given in this paper comparing radio continuum data at 3.6 and 20 cm. For the ultra-compact component, we use VLA data to obtain physical parameters at 3.6 cm confirming this region as an UC H II region. Using ALMA observations, we detect the presence of a dense (2.6×10^7 cm^{-3}) and small (~ 2.0 arcsec; 0.08 pc) molecular clump with a mass of 220 M$_\odot$ and average kinetic temperature of 21 K, located near to the UC H II region. In this clump, catalogued as G43.890–0.784, water masers also exist, possibly tracing a bipolar outflow. We discover in this vicinity two additional clumps which we label as G43.899–0.786 ($T_d = 50$ K; $M = 11$ M$_\odot$) and G43.888–0.787 ($T_d = 50$ K; $M = 15$ M$_\odot$).

Key words: Stars: massive – H II regions – ISM: molecules – Infrared: ISM – Radio lines: ISM.

1 INTRODUCTION

The study of UC H II regions is very important to understand the high-mass star formation process because they trace regions with recently formed ionizing (OB-type) stars. The UC H II regions are often related to hot molecular cores and maser emission (e.g. Hofner & Churchwell 1996; Garay & Lizano 1999; Kurtz et al. 2000b; Churchwell 2002; de la Fuente et al. 2018; and references therein). They were identified by Wood & Churchwell (1989) and Kurtz, Churchwell & Wood (1994) as small (sizes ≤ 0.1 pc) and dense ($\gtrsim 10^4$ cm^{-3}) H II regions with high emission measures ($\geq 10^7$ pc cm^{-6}). The physical parameters of the ionized gas are determined by radio continuum (RC) and radio recombination line (RRL) observations (e.g. Oster 1961; Mezger & Henderson 1967; Schraml & Mezger 1969; Dupree & Goldberg 1970; Panagia & Walmsley 1978).

There are five *booms* in the history of the topic: (1) the original studies via single-dish observations (e.g. Mezger & Henderson 1967; Ryle & Downes 1967; Israel, Habing & de Jong 1973; and references therein), (2) the physical characterization for the first time via VLA interferometric observations (Wood & Churchwell 1989; Kurtz et al. 1994), (3) observations (and studies) of *extended emission* (EE) at arcmin scales by de la Fuente 2007 (see Kurtz et al. 1999; Kim & Koo 2001, 2002, 2003; Ellingsen, Shabala & Kurtz 2005; de la Fuente et al. 2009a, b, 2018, 2020), (4) the discovery of time variation in the radio flux density (Franco-Hernández & Rodriguez 2004; Gálvan-Madrid et al. 2008), and (5) the detection of hypercompact (HC) H II regions (Gaume et al. 1995; Sewiło et al. 2004, 2008; DePree, Wilner & Goss 2011). Reviews can be found in Kurtz (2000a), Churchwell (2002), de la Fuente et al. (2009a), and references therein.

In the morphological study performed by de la Fuente et al. (2020, Paper I hereafter), we found that extended radio continuum emission (EE) resembles bubble-like structures found in the *Bubbling Universe* revealed by *Spitzer* observations (e.g. Churchwell et al. 2006, 2007, 2009; Everett & Churchwell 2010; Simpson et al. 2012; and references therein). Paper I also shows that for all the sources of the sample, except for G12.21–0.10 (G12.21 hereafter), the *Spitzer* MIPS emission at 24 μm is saturated at the position of the UC

---

[*] E-mail: eduardo.delafuente@academicos.udg.mx
[†] Also HAWC Gamma-Ray National Laboratory (CONACyT), México. Research visit at Institute for Cosmic Ray Research (2020 February), University of Tokyo, Kashiwa Campus, Japan.

Table 1. High-resolution radio continuum observations.[a]

| λ (cm)	Instrument	S_ν[b] (mJy)	Beam size (arcsec × arcsec)	PA (°)	Source size[c] (arcsec)	rms (mJy beam^{-1})	Observational program
0.3	ALMA	401.0	1.90 × 1.58	+ 57.0	2.29	0.30	2015.1.00280.S
0.3	OVRO	260.0	3.45 × 2.45	−58.0	1.70	3.00	–
0.7	VLA–CnB	396.0	1.46 × 0.81	+ 90.0	2.00	0.80	AK423
2.0	VLA–CnB	420.0	1.58 × 0.95	−08.0	2.00	0.30	AK423
3.6	VLA–CnB	570.0	2.86 × 1.85	−08.0	3.20	0.20	AK423

[a]Technical details of the low-resolution VLA observations (the 20 cm NVSS data) are given in Condon et al. (1998).
[b]Uncertainty on integrated flux is 20 per cent at 0.3 and 0.7 cm; 10 per cent at 2 cm; 5 per cent at 3.6 cm; and 10 per cent at 20.0 cm.
[c]Deconvolved size obtained using the task *imfit* of AIPS; $\Theta_s = \sqrt{\Theta_x \Theta_y}$.

Table 2. Parameters of the spectral-line observations.

Line	Instrument	Rest frequency (GHz)	Channel width (km s^{-1})	rms (mJy beam^{-1})	Beam size (arcsec × arcsec)	PA (°)
H40α	ALMA	99.02296	3.0	1.5	1.68 × 1.34	+ 66
H41α	OVRO	92.03444	3.3	25.0	3.45 × 2.45	−58
H42α	ALMA	85.68839	3.0	2.0	1.92 × 1.68	+ 64
$^{13}CS(J = 2\rightarrow1)$	OVRO	92.49431	1.6	35.0	3.45 × 2.45	−58
CS($J = 2\rightarrow1$)	ALMA	97.98095	3.0	2.0	1.67 × 1.43	+ 68
HCN($J = 1\rightarrow0$)	ALMA	88.63160	3.0	2.0	1.86 × 1.63	+ 59
H^{13}CN($J = 1\rightarrow0$)	ALMA	86.33992	3.0	2.0	1.91 × 1.65	+ 62
HCO$^+$($J = 1\rightarrow0$)	ALMA	89.18852	3.0	2.0	1.85 × 1.63	+ 60
SiO($J = 2\rightarrow1$)	ALMA	86.84696	3.0	2.0	1.89 × 1.65	+ 62
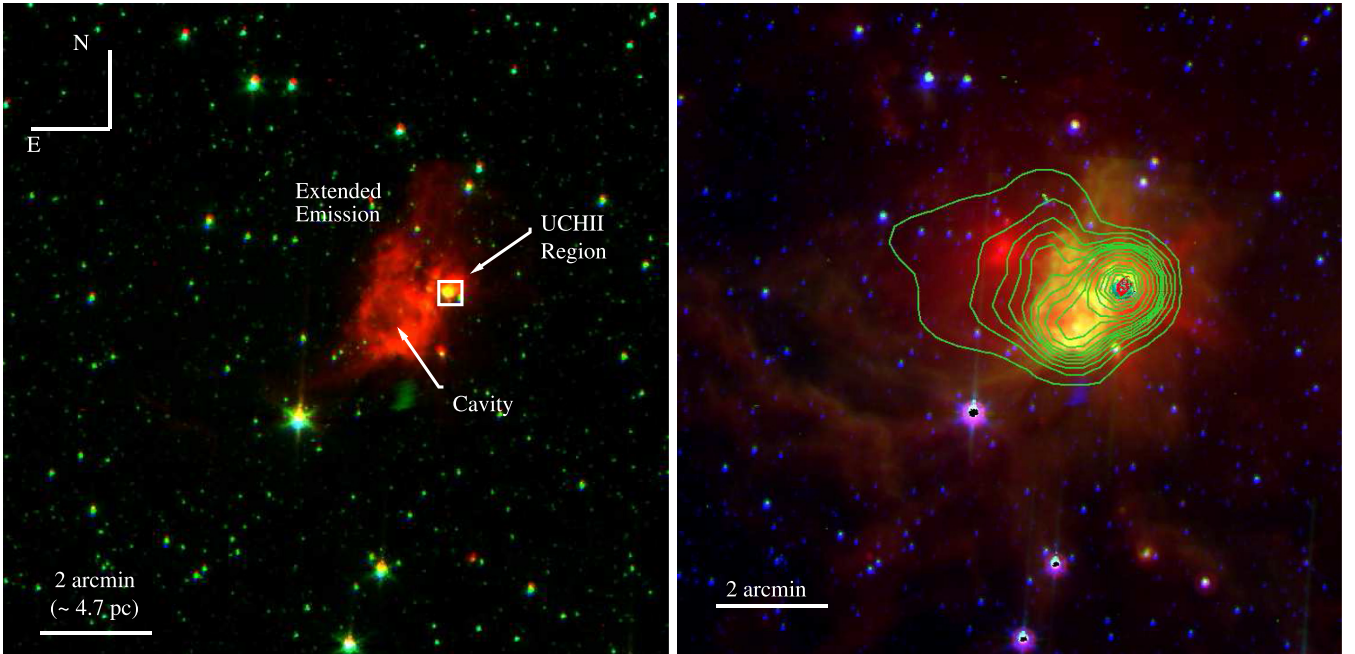
Figure 1. G43.89–0.78. Left: *Spitzer* IRAC RGB (8 + 4.5 + 3.6 μm) image. The red emission traces the extended emission. The square shows the position of the UC H II region. A cavity-like structure is marked. The yellow emission at the position of the UC H II region is from the intense 4.5 μm emission. This emission is clearly observed in its corresponding IRAC image, and matches very well with the red emission. Right: *Spitzer* IRAC+MIPS RGB (24 + 8 + 4.5 μm) image. Green contours are from NVSS showing the 20 cm emission tracing extended ionized gas. The levels are −4, 4, 8, 16, 32, ... times 1.20 mJy beam^{-1}. The NVSS peak emission, at the position of the UC H II region, is coincident with the emission at 3.6 cm (red contours). In this small region, also 24 μm emission is saturated (cyan colour). The emission at 4.5 and 8 μm, shown here in yellow, matches with higher values of NVSS contours. The NVSS emission has two peaks, one related with the UC component (peak 1), and other related with the cavity (peak 2). At a distance of 8 kpc, 2 arcmin corresponds to ∼4.7 pc.

component (the UC H II region). Hence, this MIPS band could be a good tracer of UC H II regions and especially those UC H II with EE (UC H II + EE regions) via visual inspection. Such infrared data could thus be an important complement to morphological studies by

avoiding the spatial filtering of extended emission inherent to radio-interferometers. Water maser emission is known to be a common – if not ubiquitous – phenomenon in star formation regions (e.g. Elitzur 1992; Garay & Lizano 1999; Trinidad et al. 2003; Codella et al.
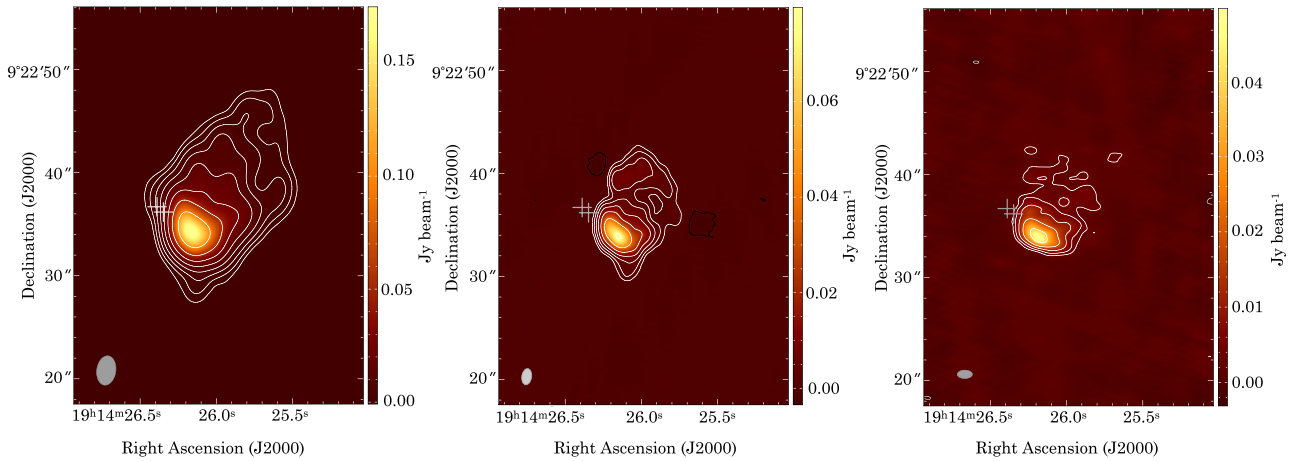
Figure 2. Radio continuum emission for G43.89–0.78 at 3.6, 2, and 0.7 cm observed with the VLA at high resolution. The contours increase as $\pm 4 \times$ rms $\times$ 2^i with $i = 0, 1, 2, 3\ldots$ (black contours have negative values) and the rms is listed in Table 1. The synthesized beams (see Table 1) are shown in the bottom left-hand corner of each panel. The crosses mark the position of the water masers from Hofner & Churchwell (1996). These maps trace only the UC component.

2004; and references therein). Nevertheless, various questions remain regarding the relation of the masers to the star formation process. Hofner & Churchwell (1996) show that for UC H II regions with cometary morphologies, water masers are always located in clumps, near, but offset from, the cometary arc. These masers could be related to nearby, embedded young stellar objects rather than to the H II regions themselves.

G12.21 and G43.89–0.78 (G43.89 hereafter) are good candidates to study the nature of these water maser clumps because these two sources have larger separations between the masers and the H II region. Hence, the maser clump can be spatially resolved from ionized gas. In this context, the molecular clump with water masers observed in the UC component of the UC H II + EE region G12.21 was characterized as a hot molecular core via NH$_3$ (2,2) and (4,4) VLA observations by de la Fuente et al. (2018). These authors start their analysis with the detection of ^{13}CS(2–1) at the position of the water masers. They confirm that the masers arise within the molecular core instead of the H II region. A similar analysis was not performed for G43.89; hence, the origin of the masers remained unknown for this source. The purpose of the present paper is to provide such an analysis for G43.89 and further, elucidate the origin of water masers during the star formation process.

G43.89 (IRAS 19120 + 0917) is a cometary UC H II region with a diameter of ~ 4 arcsec (Wood & Churchwell 1989). Its distance is uncertain. Wink, Altenhoff & Mezger (1982) via H76α observations ($V_{\mathrm{LSR}} = 50.9$ km s^{-1}) find near/far kinematic distances of 3.9/10.5 kpc. Using the CS velocity of V_{LSR} of 54.2 km s^{-1} reported by Bronfman, Nyman & May (1996) and the galactic rotation model of Wouterloot et al. (1990), we estimate near and far kinematic distances of 6.5 and 8.0 kpc, respectively. Kuchar & Bania (1990) report H I absorption up to the terminal velocity, and adopt a distance of 8.8 kpc. Araya et al. (2002) found a distance of 8.12 kpc. Wenger et al. (2018) report a Monte Carlo parallax distance of 7.82 kpc. We adopt 8.0 kpc as the distance to G43.89 for our analysis.

The water maser emission towards G43.89 was first detected by Churchwell, Walmsley & Cesaroni (1990) and mapped with high spatial resolution by Hofner & Churchwell (1996). CH$_3$OH maser emission at 6.67 GHz was reported by Schutte et al. (1993). Baudry et al. (1997) and Codella et al. (2010) suggest the presence of OH maser emission. The NH$_3$ (1,1), (2,2), and (3,3) observations

of Codella et al. (2010) show weak emission with no distinctive morphology. CS studies were performed by Hatchell et al. (1998) and Olmi & Cesaroni (1999). Bronfman et al. (1996) detected emission of CS($J = 2 \rightarrow 1$). Single-dish C$_2$H$_3$N and NH$_3$ observations by Olmi, Cesaroni & Walmsley (1993) indicate a gas temperature T~ 30 K. The high-excitation NH$_3$ studies of Cesaroni, Walmsley & Churchwell (1992) and Olmi et al. (1993) indicate the presence of hot, dense gas, but Hatchell et al. (1998, 2000) find no evidence for a hot molecular core. Single-dish CO observations by Shepherd & Churchwell (1996) detect a total linewidth of 39.1 km s^{-1} that suggests an outflow. Infrared fluxes were measured and spectra taken by Doherty et al. (1994) and Hanson, Luhman & Rieke (2002).

Here, we perform a study of G43.89 similar to that of G12.21 by de la Fuente et al. (2018). Our goals are to investigate where the water masers arise and to characterize both the ionized and molecular gas components of G43.89. In Section 2, we describe the observations and data reduction procedures. Results and discussion are given in Section 3. Summary and conclusions are given in Section 4. The physical characterization at 3.6 cm for UC H II + EE regions of Paper I and the comparison with the Kim & Koo (2001) study at 20 cm is shown in the Appendix. The latter helps to confirm G43.89 as an UC H II + EE region.

2 OBSERVATIONS

2.1 *Spitzer* and low-resolution VLA observations

Infrared observations were taken from the *Spitzer* telescope (Werner et al. 2004) Legacy Programs. IRAC (Fazio et al. 2004) data from the GLIMPSE *Spitzer* and Ancillary Data (Benjamin et al. 2003) and MIPS (Rieke et al. 2004) 24 μm data from MIPSGAL (Carey et al. 2009) were retrieved.

The IR imagery traces extended emission of UC H II regions at arcmin scales. The stellar content and PAHs at 3.3 μm are observed in the [3.6] μm IRAC1 band. The ionized gas is detected in the [4.5] μm IRAC2 band. The [5.8] μm IRAC3 band traces cold dust and PAHs at 6.2 μm. The [8.0] μm IRAC4 band traces PAHs where the 7.7 μm emission is predominant. The MIPS [24] μm band detects warm dust and embedded YSOs as point-like sources. More details and a description of characteristics in these bands in UC H II + EE regions is presented in Paper I (and references

Table 3. Results for the ionized gas.

H II	S_ν	Distance	Source size	Source	$T_e{}^a$	EM	n_e	$M_{H II}$	$\log(N_c')$	Spectral[b]
Component	(mJy)	(kpc)	(arcsec)	size (pc)	(K)	(cm^{-6} pc)	(cm^{-3})	M$_\odot$	(s^{-1})	type (radio)
Extended emission	318[c]	8.0	45.0	1.75	10000	8.7×10^4	2.2×10^2	16.00	48.10	O9
Ultracompact	570[d]	8.0	3.2	0.12	10700	3.7×10^7	1.8×10^4	0.43	48.44	O8

[a]We adopt the canonical value of 1×10^4 K for the EE, and for the UC we use the electron temperature derived from the H41α emission using equation (1) with values from Table 2).

[b]Using Panagia (1973). All sources considered at ZAMS.

[c]This flux corresponds to the NVSS peak 1 only.

[d]This flux corresponds to the VLA CnB conf. at 3.6 cm.
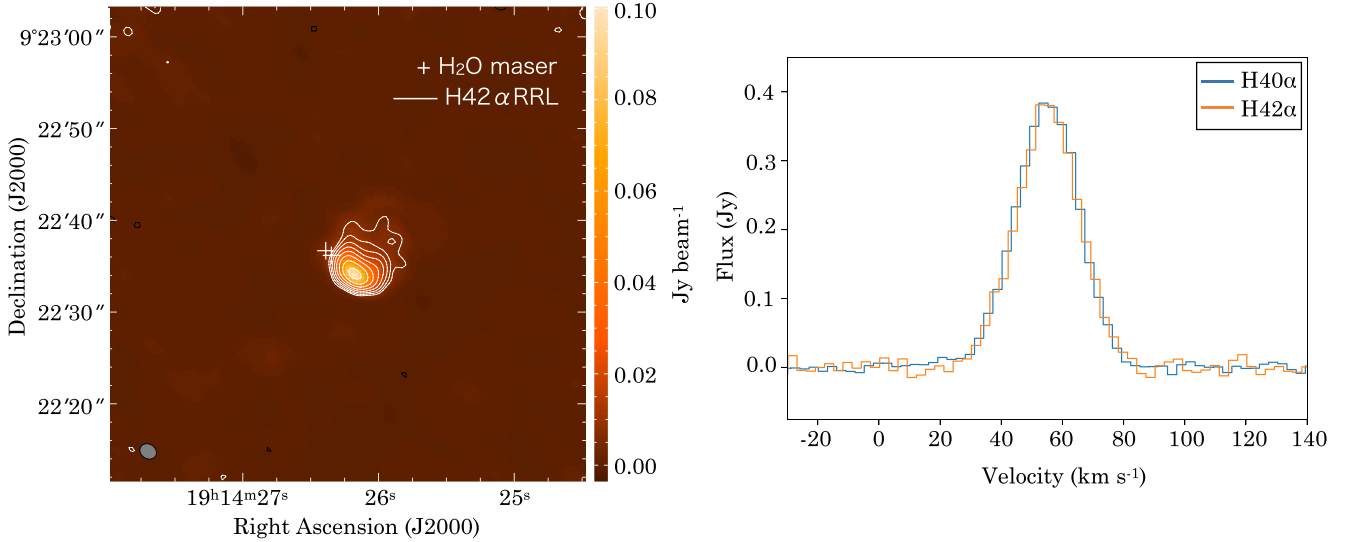
Figure 3. Continuum at $\nu \sim 92.856$ GHz and RRL emission of G43.89–0.78 obtained from ALMA observations. Left: The colour map corresponds to the continuum emission at 0.3 cm and the contours represent the velocity-integrated emission of the H42α line obtained by integrating emission in the velocity range from ~ 0 to 100 km s^{-1}, ensuring that all the line is included. The contours increase as $\pm 5 \times$ rms $\times 1.5^i$ with $i = 0, 1, 2, 3 \ldots$ (black contours have negative values) and the rms is listed on Table 2. The synthesized beam (see Table 2) is shown in the bottom left-hand corner. The crosses mark the position of the water masers from Hofner & Churchwell (1996). Right: Continuum subtracted line profiles of the H40α and H42α emissions.

Table 4. Results of the RRL observations.

Line	$S_\nu{}^a$	Size[b]	V_{LSR}	ΔV (FWHM)	T_L/T_C
	(mJy)	(arcsec)	(km s^{-1})	(km s^{-1})	(at 0.3 cm)
H40α	386.0	2.2	55.2 ± 0.1	24.4 ± 0.2	0.95 ± 0.01
H41α	246.0	3.0	56.6 ± 0.4	25.8 ± 0.9	0.95 ± 0.02
H42α	378.0	2.4	55.3 ± 0.1	24.3 ± 0.3	0.95 ± 0.01

[a]Uncertainties on integrated flux are 20 per cent. Typical OVRO beam sizes for the 0.3 cm lines are 3 arcsec. Uncertainties on integrated flux for ALMA observations are 5 per cent.

[b]Deconvolved size obtained from observations using task *imfit* of AIPS. $\Theta_s = \sqrt{\Theta_x \Theta_y}$.

therein) (see also Robitaille et al. 2006, 2008; de la Fuente et al. 2009a, b).

Because there are no VLA observations at 3.6 cm in configurations C or D for G43.89, we follow Kurtz et al. (1999) and use 20 cm NVSS observations from Condon et al. (1998) to trace the EE. NVSS has a sensitivity to structures 7–15 arcmin, and the EE seems to be associated with IR *Spitzer* bubbles (see Paper I), with the NVSS emission encompassing the arcminute-scale IR structures.

2.2 High-resolution observations

2.2.1 VLA and OVRO observations

VLA observations of RC at 0.7, 2, and 3.6 cm towards G43.89 were performed simultaneously with those of G12.21, reported by de la Fuente et al. (2018). In a similar way to G12.21, we used the Owens Valley Radio Observatory (OVRO) Millimeter Array to observe RC emission at 0.3 cm, and the ^{13}CS($J = 2 \rightarrow 1$) ($\nu_0 = 92.49430$ GHz) line and the H41 α ($\nu_0 = 92.03445$ GHz) line emission towards G43.89. The observations were carried out in March and April, 1996, using both equatorial and high-resolution configurations. Details of these observations, instrumental set-up, calibration, and data reduction procedures are presented in de la Fuente et al. (2018).

Calibration and standard data reduction procedures were performed using the AIPS package.[1] Observational parameters for the high-resolution RC are shown in Table 1. Table 2 gives the corresponding parameters for the spectral-line observations.

---

[1]AIPS is produced and maintained by the National Radio Astronomy Observatory, a facility of the National Science Foundation operated under cooperative agreement by Associated Universities, Inc.
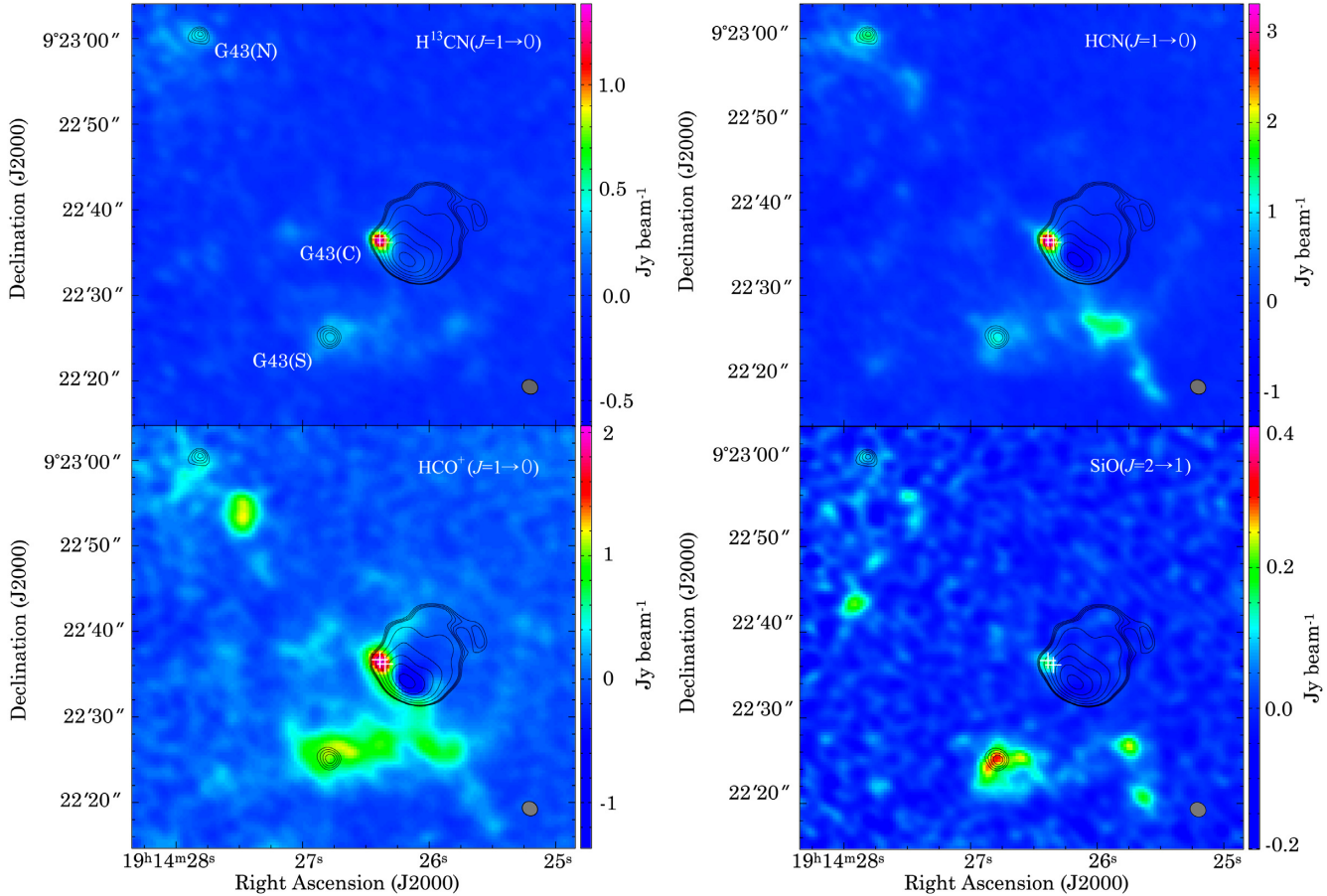
Figure 4. ALMA observations of the continuum emission as well as line emission of different molecular species in the vicinity of G43.89−0.78. The black contours represent the continuum emission at 0.3 cm. The first four contours are 5, 6, 7, and 8 times the rms of the map (listed in Table 2) and then they increase as $\pm 8 \times$ rms $\times 2^i$ with $i = 0, 1, 2, 3, \ldots$. Apart from the cometary UC H II region, three other continuum clumps were identified and they are indicated in the upper left-hand panel as G43(N), G43(C), and G43(S) (see the main text). The water masers from Hofner & Churchwell (1996) are marked as white crosses.

2.2.2 ALMA observations

We retrieved archival Atacama Large Millimetre Array (ALMA) data of the project 2015.1.00280.S (PI: R. Cesaroni) to study the molecular, mm-continuum, and RRL emission associated with G43.89. The observations were performed using Band 3 (84–116 GHz) receivers and include two Executions Blocks (EBs) obtained on 2016 March 16 and 17 with 37 and 40 12-m antennas, respectively.

A total of six spectral windows with different bandwidths and spectral resolutions were used to target the continuum and line emission.

The highest and lowest spectral resolutions of the observations are 0.42 and 1.48 km s^{-1}, respectively. The total observation time on G43.89 was 35 min (including both EBs). The baselines of the array covered a range from 15.1 to 460.0 m, which provided an angular resolution of ∼1.5 arcsec and a maximum recoverable scale of ∼25 arcsec.

Precipitable water vapour levels ranged from 2.3 to 2.9 mm and the typical system temperature was 50–100 K for different antennas. The data were calibrated with the ALMA pipeline (36252–Pipeline-Cycle3-R4-B; CASA version 4.5.2 r36115) using J1751+0939 (∼2.72 Jy at 86.751 GHz) as a flux/bandpass calibrator and J1922+1530 ∼ 260 mJy as a gain calibrator.

Images were created using Briggs weighting with the robust parameter set to −0.5 in order to improve the spatial resolution,

at the cost of slightly higher noise. The 0.3 cm continuum image has an average rms of 0.3 mJy beam^{-1}. The corresponding molecular line observational parameters are summarized in Table 2.

3 RESULTS AND DISCUSSION

We study the EE associated with G43.89 via *Spitzer* and VLA low-resolution observations. The need for this study was evident upon visual inspection of the MIPS image, which shows significant structure around the saturated UC H II region.

3.1 The extended emission

IRAC and IRAC+MIPS RGB images for G43.89 are shown in Fig. 1. The IRAC morphology is similar to other UC H II + EE regions shown by de la Fuente et al. (2009a, b) with the EE marked by the red emission at 8.0 μm. In G43.89, the emission at 4.5 μm is considerable and matches the south-western edge of the 8 μm morphology (in red), being more intense at the position of the UC H II region (in yellow) marked with a square in Fig. 1 (left). An almost circular structure with size ∼ 1 arcmin, considered as a cavity, is seen at 8 μm and delineates a bubble-like shape that is characteristic of some star-forming regions in the Milky Way (Churchwell et al. 2006) as revealed by *Spitzer* observations.
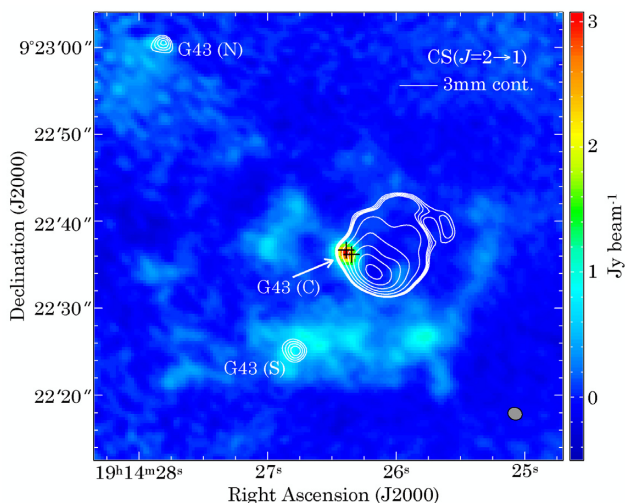
Figure 5. Continuum emission in G43.89−0.78 obtained from the ALMA observations. The colour map corresponds to the velocity-integrated CS($J = 2 \rightarrow 1$) emission integrated over the velocity range $15 < V$ (km s^{-1}) < 95. The rms of the image is 8.5×10^{-2} Jy beam^{-1} · km s^{-1}. The contours represent the continuum emission at $\nu \sim 92.856$ GHz. The first four contours are 5, 6, 7, and 8 times the rms of the map (listed on Table 2) and then they increase as $8 \times$ rms $\times 2^i$ with $i = 0, 1, 2, 3, \ldots$. The ellipse at the bottom right corner represents the size of the synthesized beam given in Table 2. The positions of the water masers reported by Hofner & Churchwell (1996) are indicated with black crosses and coincide with the molecular clump labelled as G43(C). Two extra radio-continuum clumps labelled as G43(N) and G43(S) are observed in the field.

The IRAC+MIPS image shows the same behaviour observed in UC H II + EE regions from Paper I, showing a remarkable similarity with G37.55–0.11. In both sources, low-resolution RC contours coincide with the 24 μm emission; a well-traced cavity is evident at 8 μm, which is filled with 24 μm emission, and red, point-like sources, YSOs or dust condensations, are located inside. Red contours, coinciding with the saturation at 24 μm (cyan colour), are from the high-resolution VLA 3.6 cm image, also shown in Fig. 2. This emission traces the UC component.

The NVSS emission has two peaks, one coinciding with the UC H II region position (peak 1), the other coinciding with the IRAC *cavity* (peak 2). Weaker RC emission extends to the NE as part of a larger structure of ionized gas. It is noticeable that at larger scales, the RC emission matches with 24 μm emission but does not have an IRAC counterpart (such behaviour is also seen in G37.55–0.11). The IRAC emission at 4.5 μm in peak 1 matches with the yellow emission on the IRAC+MIPS image, supporting the presence of ionized gas at several scales from the UC H II regions.

Following Kurtz et al. (1999), we see that for both the extended and the compact emission (the former traced by NVSS, the latter by the 0.7, 2, and 3.6 cm images), there is continuity at the peak-1 position (see Figs 1 and 2). Moreover, a result from Paper I is that 24 μm emission coincides with the RC emission at 3.6 cm at several scales – including the saturated UC component. This MIPS emission could indicate the presence of ionized gas at intermediate scales between the VLA high-resolution and low-resolution observations. VLA observations at 3.6 cm in the C or D-configuration could confirm this. MIPS emission at peak 1 is between 20 arcsec (the saturated zone) and 70 arcsec (including first Airy ring), in agreement with the size of 45 arcsec (1.75 pc) obtained from the NVSS image. The physical parameters of the EE and the UC H II are determined

in the standard way (equations A1–A4 in the Appendix), and these results are shown in Table 3.

These physical parameters agree with those reported in Table A1 for sources in Paper I and Kim & Koo (2001) as shown in the Appendix. Considering the calculated values and the morphological study described above, G43.89–0.78 can be catalogued as an UC H II + EE. However, intermediate resolution VLA observations at 3.6 cm, such as those presented in Paper I, would be useful to strengthen this result.

García-Segura & Franco (1996) show that wind-driven bubbles formed by the expansion of the UC H II regions produce structures that are not larger than a scale of ∼2 pc. From Fig. 1, it is clear that the RC emission of the UC H II in G43.89 extends beyond ∼4 pc. Therefore, it is likely that the expansion of a bubble driven by a wind cannot be applied to explain all of the *Spitzer* bubbling structures observed nearby G43.89.

On the other hand, star-forming regions with molecular nebulosity from the parent cloud(s) have been modelled as the result of the collision of two molecular clouds triggering massive star formation; i.e. the cloud–cloud collision (CCC) mechanism (Nagazawa & Miyama 1987; Habe & Ohta 1992). This model has been applied to giant molecular clouds turning into rich clusters of high-mass stars (e.g. Furukawa, Dawson & Ohama 2009; Ohama, Dawson & Furukawa 2010; Fukui, Ohama & Hanaoka 2014; Baug et al. 2016; Kuwahara et al. 2020), and to smaller molecular clouds that trigger the formation of clusters with one or a few (OB type) massive stars (e.g. Torii et al. 2011, 2015, 2017; Fujita et al. 2019). With high-resolution CO velocity maps, it would be viable to model emission at large scales (≳2 pc) around UC H II + EE regions with the CCC scenario.

In several cases in Paper I, we note the presence of molecular nebulosity, with the embedded UC component resembling the clump at a shocked interface between colliding clouds. The extended emission also resembles the bubble structures left behind where one or more newly formed stars ionize a cavity inside the larger cloud (*Spitzer* bubbles). Such a study could confirm if the RC morphological classification of UC H II + EE regions is related with the clouds' initial conditions, such as mass, velocity dispersion, velocity directions, and viewing angle (see Torii et al. 2015, for their 'cup' and 'tunnel' orientation discussion). In particular, for the case of G43.89, this model could explain the presence of peaks 1 and 2 in the same region.

3.2 The Ultracompact vicinity

3.2.1 RC and RRL emission

The high-resolution RC maps at 0.7, 2, and 3.6 cm, tracing the UC component, are presented in Fig. 2. These maps clearly show the cometary morphology of the UC H II region. The positions of the two water maser features reported by Hofner & Churchwell (1996) are indicated with crosses on the images. The water masers are not spatially coincident with the peak of RC observed with the VLA, but rather are offset from the head of the cometary structure. Thus, the water masers are not coincident with the ionized gas. The fact that there is 3.6 cm RC emission partially overlapping with the water masers is due to the limited angular resolution of these observations. Indeed, convolving our higher angular resolution maps at 2 and 0.7 cm with a larger beam reproduces this effect. In addition, Hofner & Churchwell (1996) mention that they found the masers to be 'well-separated' from the cometary ionized arc, which is a result of their relatively high angular resolution (∼0.5 arcsec) observations.

Table 5. Physical parameters (continuum) for clumps on G43.89 vicinity.

| Clump[a] Designation	Other[b] Designation	Right ascension (J2000:h m s)	Declination (J2000: ∘ ′ ″)	S_ν [c] (mJy)	Source[d] size (″)	T_{dust} (K)	M_{H_2} (M$_\odot$)	24 μm Counterpart
G43.899–0.786	G43 N	19 14 27.818	+ 09 23 00.33	6.00	1.34	50.00	11.00	Y
G43.888–0.787	G43 S	19 14 26.789	+ 09 22 25.12	8.00	2.60	50.00	15.00	N

Based on galactic coordinates.

[b]Respect to the main clump: G43(C) or G43.890–0.784.

[c]Integrated flux. Uncertainties of 5 per cent.

[d]Deconvolved size obtained from observations using CASA. $\Theta_s = \sqrt{\Theta_x \Theta_y}$.
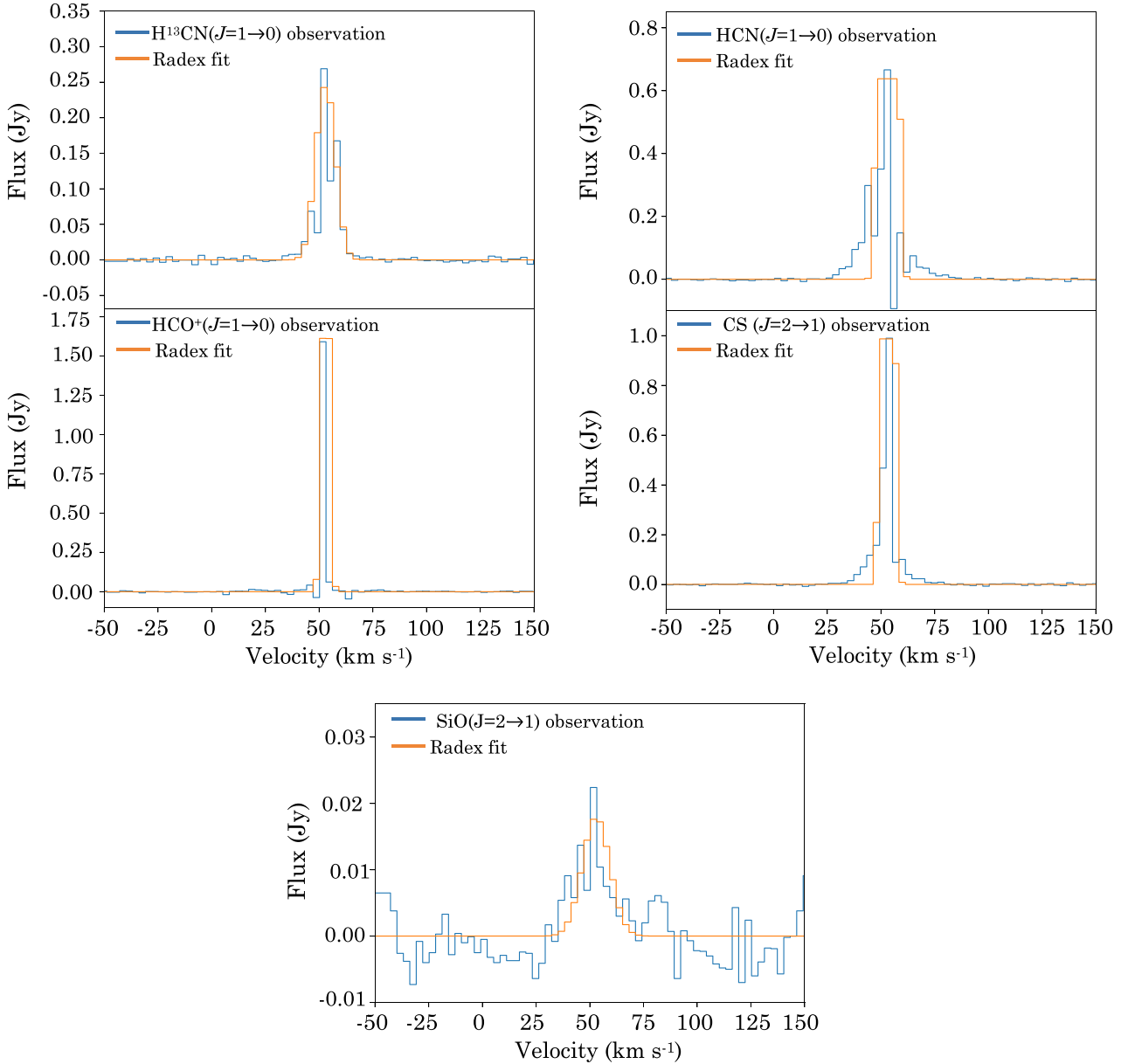
Figure 6. Spectral line profiles of different molecular species detected in G43.89(C) or G43.890–0.784. The blue lines are the ALMA observations and the orange lines are fits to the observations obtained using the RADEX in CASSIS (see Table 6 for the parameters of the fit models).

Fig. 3 shows the 0.3 cm continuum, H40α, and H42α RRL emissions obtained from ALMA observations. A contour map of the velocity-integrated H42α RRL emission, superimposed on a colour map of the continuum emission, is shown in the left-hand panel,

while the profiles of the H40α and H42α lines are shown in the right-hand panel. The velocity-integrated map of the H42α RRL was obtained by integrating emission in the velocity range from ∼0 to 100 km s^{-1}. A Gaussian fit to the profiles of the H40α and H42α

Table 6. Results of the molecular line observations of G43(C) or G43.890–0.784.

Line	Peak[a] (Jy)	V_{LSR} (km s^{-1})	ΔV (FWHM) (km s^{-1})	Column density (cm^{-2})	Abundance	Temperature (K)
^{13}CS($J=2\to1$)	<0.035	–	–	–	–	–
CS($J=2\to1$)	1.05	55.3 ± 0.1	4.0	1.00×10^{16}	5×10^{-9}	18
HCN($J=1\to0$)	0.68	55.3 ± 0.1	5.0	1.00×10^{16}	5×10^{-9}	16
H^{13}CN($J=1\to0$)	0.27	55.3 ± 0.1	10.0	1.67×10^{14}	8×10^{-11}	16
HCO$^+$($J=1\to0$)	1.60	55.3 ± 0.1	3.0	4.00×10^{15}	2×10^{-9}	35
SiO($J=2\to1$)	0.025	55.3 ± 0.1	15.0	1.60×10^{13}	8×10^{-12}	18

Notes.[a]Uncertainties on integrated flux are 20 per cent. Typical OVRO beam sizes for the 0.3 cm lines are 3 arcsec. Uncertainties on integrated flux for ALMA observations are 5 per cent.
[b]Deconvolved size obtained from observations using task *imfit* of AIPS. $\Theta_s = \sqrt{\Theta_x \Theta_y}$.
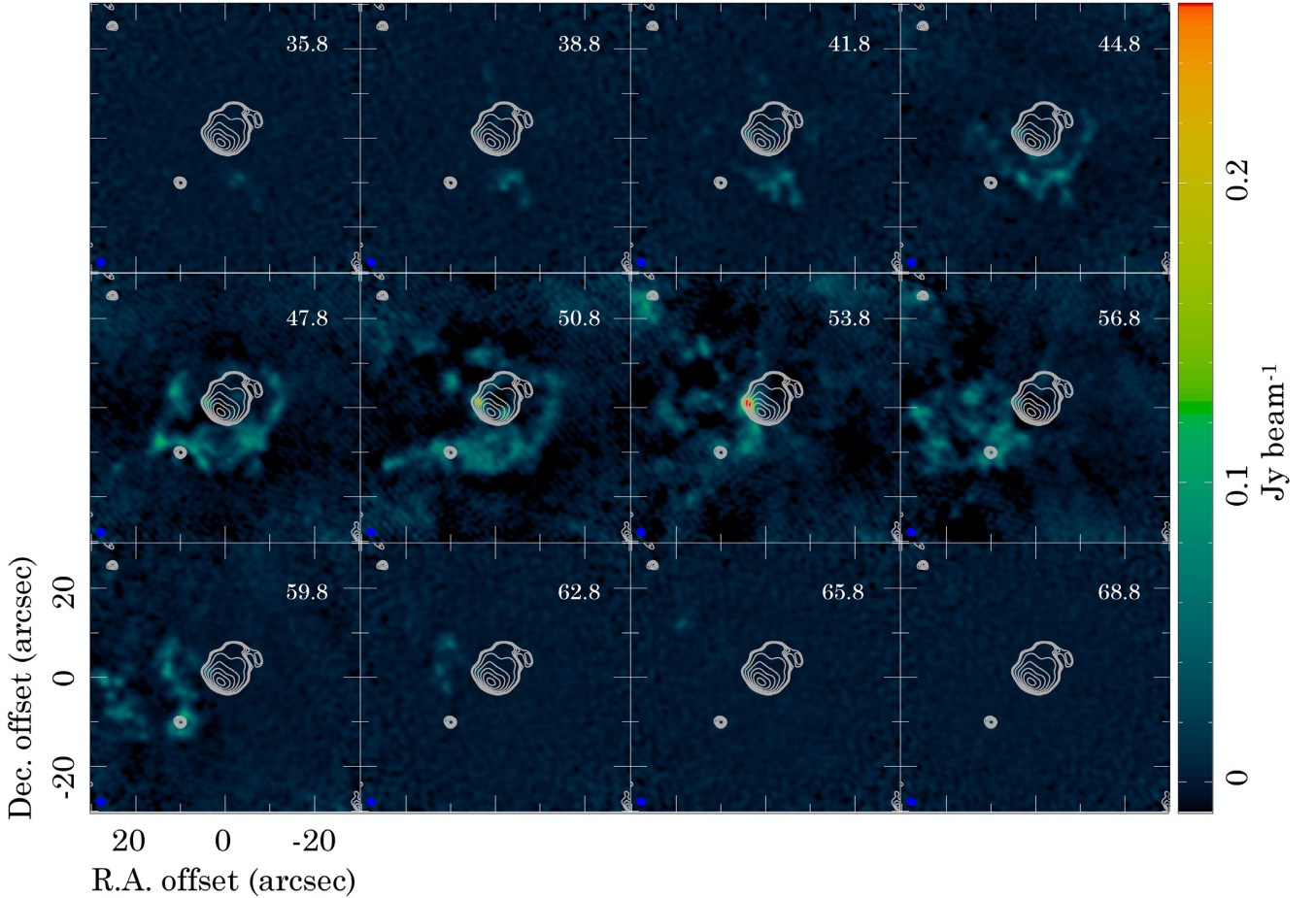
Figure 7. Channel maps of the ALMA CS emission in G43.89−0.78. The colour map is the CS($J = 2\to1$) line emission in the vicinity of G43.89−0.78 for individual channel maps. The number in the top-right corner is the velocity of the channel. The white contours represent the continuum emission at 3 mm. The first four contours are 5, 6, 7, and 8 times the rms of the map (listed on Table 2) and then they increase as $\pm 8 \times$ rms $\times 2^i$ with $i = 0, 1, 2, 3, \dots$. The synthesized beam is indicated with a blue ellipse located in the bottom left-hand corner of the individual channel maps (see Table 2).

RRLs gives a peak velocity $V_{LSR} = 55.2 \pm 0.1$ km s^{-1} and a FWHM $\Delta V = 24.3 \pm 0.3$ km s^{-1}, which is in agreement with the systemic velocity $V \sim 55$ km s^{-1} obtained from previous molecular observations (Olmi et al. 1993; Bronfman et al. 1996; Olmi & Cesaroni 1999; Araya et al. 2002). A fit to the H41α line observed with OVRO gives a similar result (see Table 4). These results indicate that the ionized gas and the molecular gas are physically associated.

From the ratio of the continuum and RRL fluxes, and the linewidth of the RRL, it is possible to determine the LTE electronic temperature,

T_e, of the ionized gas as (Mezger & Henderson 1967; Dupree & Goldberg 1970):

$$\left(\frac{T_e}{K}\right) = 2.2 \times 10^3 \left(\frac{\nu}{\text{GHz}}\right)^{0.96} \left(\frac{T_L}{T_C}\right)^{-0.87} \left(\frac{\Delta V}{\text{km s}^{-1}}\right)^{-0.87}, \quad (1)$$

where ν is the observation frequency, T_C is the brightness temperature of the continuum emission, and T_L and ΔV are the continuum-subtracted peak brightness temperature and the linewidth of the RRL, respectively. Since S_L/S_C is ~ 0.95 (see Table 4), equation (1)
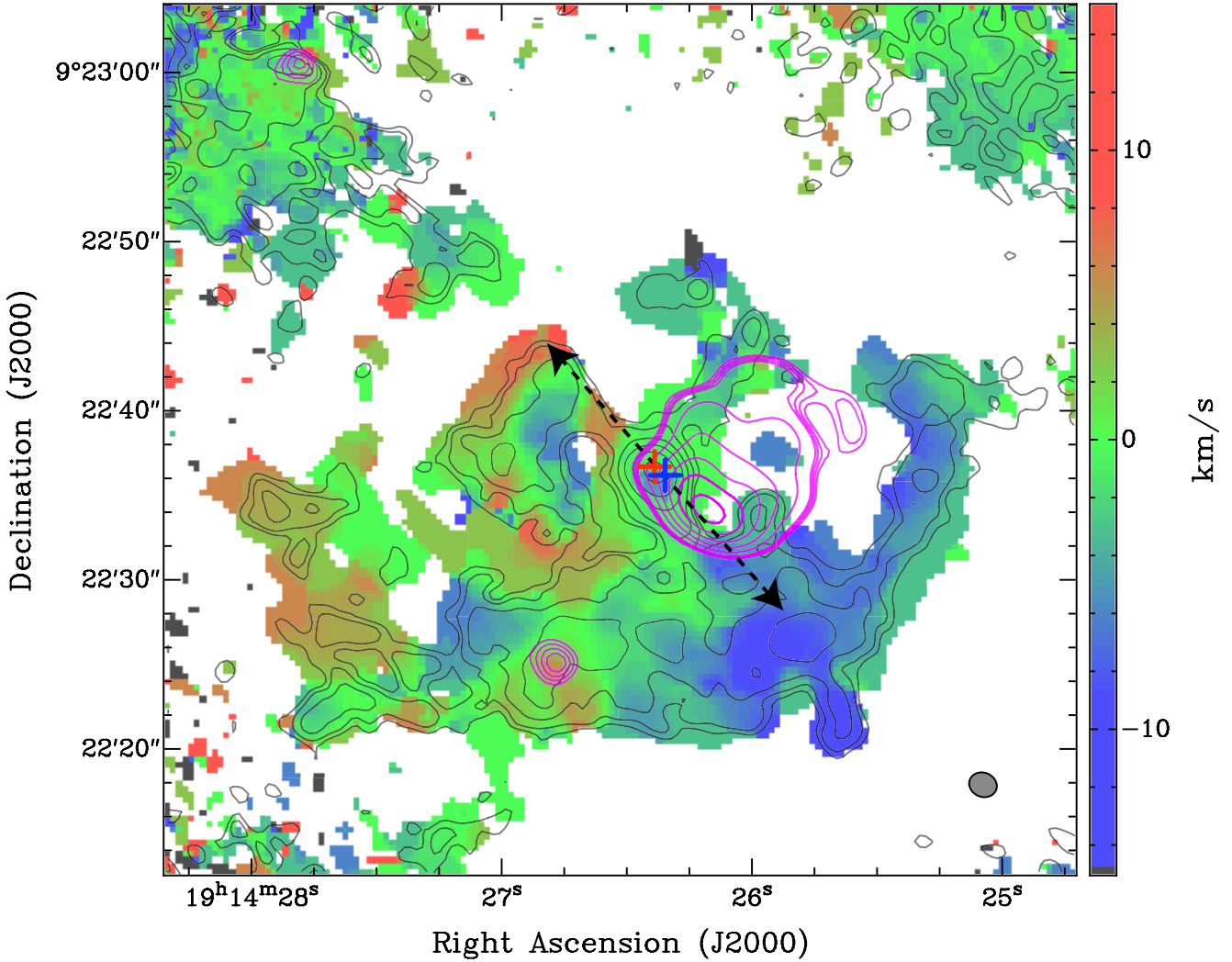
Figure 8. Moment-1 image of the CS($J = 2{\rightarrow}1$) line emission in the vicinity of G43.89−0.78. The colour map is the moment-1 (velocity field) clipped at 0.01 Jy beam^{-1} (4 times the rms noise level of the channel maps). The black contours indicate the velocity-integrated CS($J = 2{\rightarrow}1$) emission (moment-0). The contours increase as $\pm 5 \times$ rms $\times 1.5^i$ with $i = 0, 1, 2, 3, \ldots$, where the rms is 0.075 Jy beam^{-1} km s^{-1}. The magenta contours represent the continuum emission at 3 mm. The first four contours are 5, 6, 7, and 8 times the rms of the map (listed on Table 2) and then they increase as $\pm 8 \times$ rms $\times 2^i$ with $i = 0, 1, 2, 3, \ldots$. A broken line with arrows indicates the direction of a kinematical feature associated with the clump G43(C) that could be a molecular outflow (see the main text).

gives an LTE $T_e \sim 1.1 \times 10^4$ K. The physical parameters obtained for the UC H II region in G43.89, using this temperature value, are presented in Table 3. For the calculations, we used the 3.6 cm data and a deconvolved size of the source $\simeq 3$ arcsec ($\simeq 0.12$ pc). The derived values of the physical parameters for this source are in approximate agreement with those obtained by Wood & Churchwell (1989).

3.2.2 ALMA and OVRO: molecular and mm-continuum emission

Using the JCMT, Hatchell et al. (1998) searched for molecular emission toward 14 UC H II regions including G43.89. For G43.89, they detected several molecular lines (C^{17}O, C^{18}O, SO, C^{34}S) and weak emission from the lowest excitation energy lines of CH$_3$CCH and CH$_3$OH. Also, Li et al. (2015) searched for sulphur-bearing molecules, including OCS, CS, H$_2$S, and SO; they only detected emission from SO(5_6–4_5).

From the ALMA observations, emission from CS($J = 2{\rightarrow}1$), HCN($J = 1{\rightarrow}0$), H^{13}CN($J = 1{\rightarrow}0$), HCO$^+$($J = 1{\rightarrow}0$), SiO($J = 2{\rightarrow}1$) lines were detected (see Figs 4 and 6). On the other hand, no OVRO ^{13}CS($J = 2{\rightarrow}1$) line emission was detected above a level of 3σ ($\sigma = 0.35$ mJy beam^{-1}) towards the UC H II region. This is almost certainly due to the limited sensitivity of OVRO observations with respect to ALMA.

Aside from the UC H II region, two more radio-continuum clumps were detected in the field of view of the ALMA observations. They are marked as G43(N) and G43(S) in Figs 4 and 5. By their galactic coordinates, these sources are designated as G43.899–0.786 and G43.888–0.787, respectively. G43(N) is coincident with a 24 μm point source within the positional uncertainties. This clump could be a proto–stellar source. On the other hand, G43(S) does not have a 24 μm counterpart, although there is considerable molecular emission at its position. G43(N), in this regard, shows only weak molecular emission. Physical parameters for these clumps are reported in Table 5.

In addition, close inspection of the continuum emission associated with the UC H II region reveals that there is a bump towards the position of the water masers, which also coincides with a bright molecular clump. We label this source as G43(C) with galactic designation G43.890–0.784. Figs 4 and 5 shows that except for the SiO($J = 2{\rightarrow}1$) emission, the molecular emission peaks in G43(C). In these figures, it is clear that the water masers are associated with G43(C). The coordinates of this brightest clump are RA(J2000) = $19^{\rm h}14^{\rm m}26\overset{\rm s}{.}387$, Dec. (J2000) = $9°22'36''28$. The configuration of the cometary UC H II region with a molecular clump and water masers resembles that of G12.21, where de la Fuente et al. (2018) concluded it is a hot molecular core. Thus, in order to assess whether G43.89 also contains a hot molecular core we proceed to study the molecular clump of G43.89 in a similar way as for G12.21.

To determine the physical parameters of the molecular gas in G43(C) we used the CASSIS software, the CDMS spectroscopic data bases, the LAMDA molecular data bases, and the RADEX code.[2] We extracted spectra from all the molecular species detected with ALMA and then we fitted a model by varying parameters such as the kinetic temperature, and column densities. Fig. 6 shows the fits to the observations. The best fit gives a molecular hydrogen column density of N(H$_2$) = 2×10^{24} cm^{-2}, which translates into a volumetric density of n(H$_2$) = 2.6×10^7 cm^{-3} and a mass of M(H$_2$) = 220 M$_\odot$. The physical parameters of the best-fitting models are listed in Table 6. The kinetic temperature of the gas ranges from 16 to 35 K. The gas traced by HCO$^+$ is the warmest of all, suggesting that the emission arises closer to a proto-stellar object.

The G43(C) clump does not completely meet the operational definition of a hot molecular core given in Garay & Lizano (1999, and references therein): size $\lesssim$ 0.1 pc, $T_{\rm k} > 50$ K, and $n_{\rm e} \gtrsim 10^5$ cm^{-3}, because the reported temperature is $\lesssim$50 K. Possibly this YSO is in such an early evolutionary stage that the gas has not yet been heated by the YSO or that the dusty molecular core lacks sufficient optical depth to absorb the radiant energy. In an attempt to estimate the evolutionary stage of G43(C), we compare the physical parameters from Table 6 with the chemical models from Nomura & Millar (2004) assuming a temperature-dependent grain mantle evaporation process. An approximate timescale of 1×10^4 yr is obtained for a column density of CS 1×10^{16} cm^{-2}.

A timescale of $\sim 6 \times 10^4$ yr is obtained from HCN (see their fig. 2c). In comparison, the average column densities of some molecular tracers from hot cores given by Li et al. (2015, see their table 6) are more consistent with a CS time-scale between 6×10^4 and 1×10^5 yr, which corresponds to an older stage than for G43(C) by about an order of magnitude. This is in agreement with the chemical evolutionary sequence proposed by Beuther (2007) for hot molecular cores, where cores at $\sim$30 K cause some molecules to be released from dust grains (such as CS), but when the temperature of the hot core increases to $\gtrsim$100 K, the H$_2$O molecules released also from dust grains generate the enrichment of other molecular tracers and their abundance (e.g. SO).

We also estimated the mass of the clumps G43(N) and G43(S). For a frequency of 86 GHz, considering continuum flux densities (S_ν), and assuming emission from isothermal, optically thin dust, the gas mass can be determined using (Hildebrand 1983; Gall, Hjorth &

Andersen 2011):

$$\left[\frac{M_{\rm gas}}{M_\odot}\right] = 4.8 \times 10^{-23} \frac{g}{B_\nu(T_{\rm dust})} \left[\frac{S_\nu^{\rm N,S}}{\rm mJy}\right] \left[\frac{\kappa_\nu}{\rm cm^2 g^{-1}}\right]^{-1} \left[\frac{D}{\rm pc}\right]^2, \quad (2)$$

where g is the gas-to-dust ratio, D is the adopted distance, $\kappa_\nu^{1.3\rm mm}$ is the dust mass opacity coefficient, and $B_\nu(T_{\rm dust})$ is the Planck function for a dust temperature $T_{\rm dust}$. For a $B_\nu(T_{\rm dust})$ with $T_d = 50$ K, we derive the clump masses reported in Table 5. In this calculation, the uncertainty is only referenced to the uncertainty in the adopted value of $\kappa_\nu^{1.3\,\rm mm}$; we use 0.015 cm^2 gr^{-1}.

3.2.3 A molecular outflow from the clump G43(C)?

From the line profiles shown in Fig. 6, it can be seen that some molecular species, such as HCN and CS, exhibit wings with relatively high velocities (spanning a velocity range of $\sim$50 km s^{-1}). Such wings cannot be fitted with any Gaussian curve. Furthermore, the CS($J = 2{\rightarrow}1$) emission in the vicinity of G43.89$-$0.78 exhibits a NE–SW velocity gradient, which can be seen in Figs 7 and 8.

In particular, there is a feature that extends in the NE–SW direction that connects G43(N) with G43(C) and a clump of molecular emission located SW of G43(C). In addition, the velocity gradient of the water masers associated with G43(C) (see Fig. 8) matches the velocity gradient of the molecular emission. This suggests that G43(C) hosts a bipolar molecular outflow that may be the origin of the water masers, as has been observed in other sources (Trinidad 2009). The direction of the outflow is indicated with a broken line in Fig. 8. Further investigations with higher angular resolution, involving proper motion observations, are needed to confirm this idea and to elucidate the nature of this object.

4 SUMMARY AND CONCLUSIONS

(i) The EE associated with G43.89 meets the nominal definition of UC H II + EE regions based on physical parameters: EM $\sim 10^4$–10^5 cm^{-6} pc, n$_{\rm e} \lesssim 5 \times 10^2$ cm^{-3}, and $M_{\rm H\,II} \sim$ 5 to 10^3 M$_\odot$; therefore, it can be added to the final catalogue given in Paper I.

(ii) G43.89–0.78 is confirmed as an UC H II region using high–resolution VLA data at 3.6 cm. It has a dense (2.6×10^7 cm^{-3}), and small ($\sim$2 arcsec or 0.08 pc) nearby molecular clump with mass of 220 M$_\odot$. The water masers appear to be spatially coincident with this clump, and may arise in a molecular outflow.

(iii) The low temperature of this clump implies that it is not a hot molecular core; however, a time-scale of few times 10^4 yr is estimated by comparison with chemical models. This value is smaller than the average time-scale for typical hot cores by about an order of magnitude.

(iv) G43.890–0.784 is rich in molecular species, and we detect two new radio-continuum clumps, G43.899–0.786 and G43.888–0.787, respectively, located in its vicinity.

ACKNOWLEDGEMENTS

---

[2]CASSIS has been developed by IRAP-UPS/CNRS (http://cassis.irap.omp.eu).

DATA AVAILABILITY

The data underlying this article are available as follows:

(1) ALMA archive at https://almascience.eso.org/asax/ and can be accessed with ALMA#2015.1.00280.S (PI: R. Cesaroni).

(2) NRAO Science Data Archive [Karl Jansky VLA Database] at https://archive.nrao.edu/archive/archiveproject.jsp and can be accessed with the respective Project (Proposal) Code: AK423 (PI: S. Kurtz).

(3) IRSA NASA/IPAC Infrared Science Archive at https://irsa.ipac.caltech.edu/Missions/spitzer.html, and can be accessed by selection of GLIMPSE II (program ID =187, PI: E. Churchwell), Data Set Identification = ads/sa.spitzer#0011972096; and MIPSGAL, program IDs 20597 and 30592 (PI: S. Carey)

(4) OVRO data will be shared on reasonable request to the corresponding author (PI: S. Kurtz).

REFERENCES

Araya E., Hofner P., Churchwell E., Kurtz S., 2002, ApJS, 138, 63
Baudry A., Desmurs J. F., Wilson T. L., Cohen R. J., 1997, A&A, 325, 255
Baug T., Dewangan L. K., Ojha D. K., Ninan J. P., 2010, ApJ, 833, 85
Benjamin R. A. et al., 2003, PASP, 115, 953
Beuther H., 2007, Proc. IAU 2 Symp., 237, 148
Bronfman L., Nyman L. A., May J., 1996, A&A, 115, 81
Carey S. J. et al., 2009, PASP, 121, 76
Cesaroni R., Walmsley C. M., Churchwell E., 1992, A&A, 256, 618
Churchwell E., 2002, ARA&A, 40, 27
Churchwell E., Walmsley C. M., Cesaroni R., 1990, A&A, 83, 119
Churchwell E. et al., 2006, ApJ, 649, 759
Churchwell E. et al., 2007, ApJ, 670, 428
Churchwell E. et al., 2009, PASP, 121, 213
Codella C. et al., 2004, A&A, 417, 615
Codella C., Cesaroni R., López-Sepulcre A., Beltrán M. T., Furuya R., Testi L., 2010, A&A, 510, A86
Condon J. J., Cotton W. D., Greisen E. W., Yin Q. F., Perley R. A., Taylor G. B., Broderick J. J., 1998, AJ, 115, 1693
de La Fuente E., 2007, PhD thesis, Departamento de Física, CUCEI, Universidad de Guadalajara, México
de La Fuente E., Kurtz S. E., Kumar M. S. N., Franco J., Porras A., Kemp S. N., Franco-Balderas E., 2009a, Astrophys. Space Sci., 7, 167
de La Fuente E., et al., 2009b, Rev. Mex. Astron. Astrofis. Conf. Ser., 37, 13
de la Fuente E., Trinidad M. A., Porras A., Rodríguez-Rico C., Araya E. D., Kurtz S., Hofner P., Nigoche-Netro A., 2018, Rev. Mex. Astron. Astrofis., 54, 129
de la Fuente E., Porras A., Trinidad M. A., Kurtz S. E., Kemp S. N., Tafoya D., Franco J., Rodríguez-Rico S., 2020, MNRAS, 492, 895 (Paper I)
De Pree C. G., Wilner D. J., Goss W. M., 2011, AJ, 142, 177
Doherty R. M., Puxley P., Doyon R., Brand P. W., 1994, MNRAS, 266, 487
Dupree A. K., Goldberg L., 1970, ARA&A, 8, 231
Elitzur M., 1992, ARA&A, 30, 75
Ellingsen S. P., Shabala S. S., Kurtz S. E., 2005, MNRAS, 357, 1003
Everett J. E., Churchwell E., 2010, ApJ, 713, 592
Fazio G. G. et al., 2004, ApJS, 154, 10
Franco-Hernández R., Rodríguez L. F., 2004, ApJ, 604, L105
Fujita S., Torii K., Tachihara K., Enokiya R., 2019, ApJ, 872, 49
Fukui Y., Ohama A., Hanaoka N., 2014, ApJ, 780, 36
Furukawa N., Dawson J. R., Ohama A., 2009, ApJ, 696, L115
Gall C., Hjorth J., Andersen A. C., 2011, A&AR, 19, 43
Gálvan-Madrid R., Rodríguez L. F., Ho P. T. P., Keto E., 2008, ApJ, 674, L33
Garay G., Lizano S., 1999, PASP, 111, 1049
García-Segura G., Franco J., 1996, ApJ, 469, 171
Gaume R. A., Goss W. M., Dickel H. R., Wilson T. L., Johnston K. J., 1995, ApJ, 438, 776
Habe A., Ohta K., 1992, PASJ, 44, 203
Hanson M. M., Luhman K. L., Rieke G. H., 2002, ApJS, 138, 35
Hatchell J., Thompson M. A., Millar T., Macdonald G., 1998, A&A, 133, 29
Hatchell J., Fuller G. A., Millar T. J., Thompson M. A., Macdonald G. H., 2000, A&A, 357, 637
Hildebrand R. H., 1983, QJRAS, 24, 267
Hofner P., Churchwell E., 1996, A&A, 120, 283
Israel F. P., Habing H. J., de Jong T., 1973, A&A, 27, 143
Kim K. T., Koo B. C., 2001, ApJ, 549, 979
Kim K. T., Koo B. C., 2002, ApJ, 575, 327
Kim K. T., Koo B. C., 2003, ApJ, 596, 362
Kuchar T. A., Bania T. M., 1990, ApJ, 352, 192
Kurtz S., 2000, Rev. Mex. Astron. Astrofis. Conf. Ser., 9, 169
Kurtz S., Franco J., 2002, Rev. Mex. Astron. Astrofis. Conf. Ser., 12, 16
Kurtz S., Churchwell E., Wood D. O. S., 1994, ApJS, 91, 659
Kurtz S. E., Watson A. M., Hofner P., Otte B., 1999, ApJ, 514, 23
Kurtz S., Cesaroni R., Churchwell E., Hofner P., Walmsley C. M., in Mannings V., Boss A. P., Russell S.S, 2000, Protostars and Planets IV, University of California Santa Barbara, University of Arizona Press: Tucson, p. 299
Kuwahara S., Kazufumi T., Norikazu M., Shinji F., Mikito K., Yasuo F., 2020, PASJ, Available at: https://doi.org/10.1093/pasj/psaa017
Li J., Wang J., Zhu Q., Zhang J., Li D., 2015, ApJ, 802, 40
Mezger P. G., Henderson A. P., 1967, ApJ, 147, 471
Nagasawa M., Miyama S. M., 1987, Prog. Theor. Phys., 78, 1250
Nomura H., Millar T. J., 2004, A&A, 414, 409
Olmi L., Cesaroni R., 1999, A&A, 352, 266
Olmi L., Cesaroni R., Walmsley C. M., 1993, A&A, 276, 489
Oster L., 1961, Rev. Mod. Phys., 33, 525
Panagia N., 1973, AJ, 78, 929
Panagia N., Walmsley C. M., 1978, A&A, 70, 411
Rieke G. H. et al., 2004, ApJS, 154, 25
Robitaille T. P., Whitney B. A., Indebetouw R., Wood K., Denzmore P., 2006, ApJS, 167, 256
Robitaille T. P. et al., 2008, AJ, 136, 2413
Ryle M., Downes D., 1967, ApJ, 148, L17
Schraml J., Mezger P. G., 1969, ApJ, 156, 269
Schutte A. J., van der Walt D. J., Gaylard M. J., MacLeod G. C., 1993, MNRAS, 261, 783
Sewiło M., Churchwell E., Kurtz S., Goss W. M., 2004, ApJ, 605, 285
Sewiło M., Churchwell E., Kurtz S., Goss W. M., Hofner P., 2008, ApJ, 681, 350
Shepherd D., Churchwell E., 1996, ApJ, 457, 267
Simpson R. J. et al., 2012, MNRAS, 424, 2442
Torii K. et al., 2011, ApJ, 738, 46
Torii K. et al., 2015, ApJ, 806, 7
Torii K. et al., 2015, ApJ, 835, 142
Trinidad M. A., 2009, Astrophys. Space Sci. Proc., 13, 627
Trinidad M. A., Rojas V., Plascencia J. C., Ricalde A., Curiel S., Rodríguez L. F., 2003, Rev. Mex. Astron. Astrof..s, 39, 311
Wenger T. V, Balser D. S., Anderson L. D., Bania T. M., 2018, ApJ, 856, 52
Werner M. et al., 2004, ApJS, 154, 1
Wink J. E., Altenhoff W. J., Mezger P. G., 1982, A&A, 108, 277
Wood D. O. S., Churchwell E., 1989, ApJS, 69, 831
Wouterloot J. G., Brand J., Burton W. B., Kwee K. K., 1990, A&A, 230, 21

APPENDIX: PHYSICAL PARAMETERS (3.6 CM) OF UC H II REGIONS WITH EXTENDED EMISSION

To obtain the physical parameters of the ionized gas, we assume an isothermal, pure hydrogen, homogeneous, spherically symmetric (radius r and size Θ_S), optically thin H II region, with a distance D from the Sun and electronic temperature T_e. The emission measure (EM), electronic density (n_e), the mass of the ionized gas ($M_{H II}$), and the total rate of emission of Lyman continuum photons of the ionizing star (N'_c) were calculated in the standard way using equations (A1) to (A4) (Oster 1961; Schraml & Mezger 1969; Panagia & Walmsley 1978; Kurtz et al. 1994). The spectral type was obtained using Panagia (1973).

The physical parameters of UC H II + EE regions from Paper I are shown in Table A1. For them, the total rate of emission of Lyman continuum photons and ionizing star type are shown in Paper I. For these UC H II + EE regions, values are size ~ 1–4 arcmin (~1–14 pc), EM ~ 10^4–10^5 cm^{-6} pc, $n_e \lesssim 5 \times 10^2$ cm^{-3}, and $M_{H II} \lesssim 10^3$ M$_\odot$. The values reported by Kim & Koo (2001) at 20 cm are size ~ 1–13 arcmin (~3–19 pc), EM ~ 10^4 cm^{-6} pc, $n_e \lesssim 10^2$ cm^{-3}, and $M_{H II} \sim 10^2$ to 10^3 M$_\odot$. Combining both samples, we confirm UC H II + EE regions are H II regions with these values: sizes ~1–10 arcmin (~1–20 pc), EM ~ 10^4–10^5 cm^{-6} pc, $n_e \lesssim 5 \times 10^2$ cm^{-3}, and $M_{H II} \sim 5$ to 10^3 M$_\odot$.

Table 1 of Kurtz & Franco (2002) summarizes the physical parameters of several types of H II regions. Updating with information from the 3.6 cm observations, we show an adaptation of this table, including UC H II + EE regions in Table A2:

$$\left(\frac{n_e}{cm^{-3}}\right) = 7.8 \times 10^3 \left(\frac{\nu}{4.9\,GHz}\right)^{0.05} \left(\frac{S_\nu}{mJy}\right)^{0.5} \left(\frac{T_e}{10^4\,K}\right)^{0.175}$$
$$\times \left(\frac{\Theta_s}{arcsec}\right)^{-1.5} \left(\frac{D}{kpc}\right)^{-0.5}, \quad (A1)$$

$$\left(\frac{EM}{cm^{-3}}\right) = 4.4 \times 10^5 \left(\frac{\nu}{4.9\,GHz}\right)^{0.1} \left(\frac{S_\nu}{mJy}\right) \left(\frac{T_e}{10^4\,K}\right)^{0.35}$$
$$\times \left(\frac{\Theta_s}{arcsec}\right)^{-2}, \quad (A2)$$

$$\left(\frac{M_{H II}}{M_\odot}\right) = 3.7 \times 10^{-5} \left(\frac{\nu}{4.9\,GHz}\right)^{0.05} \left(\frac{S_\nu}{mJy}\right)^{0.5} \left(\frac{T_e}{10^4\,K}\right)^{0.175}$$
$$\times \left(\frac{\Theta_s}{arcsec}\right)^{1.5} \left(\frac{D}{kpc}\right)^{2.5}, \quad (A3)$$

$$\left(\frac{N'_c}{s^{-1}}\right) \geq 8.04 \times 10^{46} \left(\frac{T_e}{K}\right)^{-0.85} \left(\frac{r}{pc}\right)^3 \left(\frac{n_e}{cm^{-3}}\right)^2. \quad (A4)$$

Table A2. Physical parameters of H II regions from radio observations. The ultracompact H II region with extended emission (UC H II + EE) category is added for the first time using 3.6 cm data.

Class of H II region	Size (pc)	EM (cm^{-6} pc)	n_e (cm^{-3})	$M_{H II}$ M$_\odot$
Hypercompact	~0.003	$\gtrsim 10^{10}$	$\gtrsim 10^6$	~10^{-3}
Ultracompact	$\lesssim 0.1$	$\gtrsim 10^7$	$\gtrsim 10^4$	~ 10^{-3}
Compact	$\lesssim 0.5$	$\gtrsim 10^7$	$\gtrsim 5 \times 10^3$	~1
UC H II + EE	1–20	10^4–10^5	$\lesssim 5 \times 10^2$	5–10^3
Classical	~10	~10^2	~100	~ 10^5
Giant	~100	~5×10^5	~10	10^3–10^6
Supergiant	$\gtrsim 100$	~10^5	~10	10^6–10^8

Table A1. Physical Parameters of the UC H II + EE regions reported in table 7 of Paper I, using RC observations at 3.6 cm[a].

Source name	S_ν[a] (Jy)	Source size [b] (arcmin)	Source size[b] (pc)	EM (10^4 cm^{-6} pc)	n_e (cm^{-3})	$M_{H II}$ (M$_\odot$)
G05.48–0.24	1.18	2.45	3.10	2.50	40.80	1799.55
G05.97–1.17	8.06	2.65	2.08	14.80	218.40	81.96
G10.30–0.15	5.80	2.45	4.28	12.50	139.80	454.96
G12.21–0.10	1.30	3.46	13.59	1.40	26.30	2745.07
G18.15–0.28	4.20	2.83	3.46	6.76	114.50	197.04
G19.60–0.23	4.33	1.26	1.28	35.18	428.80	37.68
G23.44–0.21	1.16	2.00	5.24	3.74	69.20	413.54
G23.71+0.17	1.49	2.00	5.18	4.80	78.90	455.77
G25.71+0.04	0.68	3.46	9.36	0.73	22.90	782.00
G28.20–0.05	0.48	1.50	3.97	2.75	68.20	177.62
G31.39–0.25	0.65	1.94	5.02	2.23	54.50	287.59
G35.20–1.74	11.31	2.00	1.92	3.65	112.80	33.24
G37.55–0.11	0.93	2.00	5.76	3.00	59.10	469.90
G37.87–0.40	4.11	1.00	2,71	53.00	362.50	298.72
G45.07+0.13	0.73	1.00	1.75	9.42	190.20	42.09
G45.12+0.13	1.80	1.50	2.62	10.32	162.60	121.42
G45.45+0.06	4.50	2.00	3.49	14.51	166.90	295.57
G54.10–0.06	0.52	2.45	5.63	1.12	36.50	270.99
G60.88–0.13	0.49	1.73	1.11	2.11	113.10	6.39
G77.96–0.01	0.95	2.45	3.14	2.04	66.10	84.80
G111.28–0.66	0.30	2.50	1.82	0.62	47.80	11.95

[a]We use the VLA conf. D data for all sources except G60.88–0.13 (conf. C). See Paper I for details. In this computing, we assume the canonical value for electron temperatures of 1×10^4 K for all sources. Distances are reported on table 1 of Paper I. The ionizing photon rates and spectral types are shown in table 7 of Paper I.
[b]Size $= \sqrt{\Theta_x \Theta_y}$. The values of Θ_x and Θ_y were obtained from table 5 of Paper I.

This paper has been typeset from a TEX/LATEX file prepared by the author.